Article

Surface Hydrides on Fe$_2$P Electrocatalyst Reduce CO$_2$ at Low Overpotential: Steering Selectivity to Ethylene Glycol

Karin U. D. Calvinho,[⊥] Abdulaziz W. Alherz,[⊥] Kyra M. K. Yap,[⊥] Anders B. Laursen, Shinjae Hwang, Zachary J. L. Bare, Zachary Clifford, Charles B. Musgrave,* and G. Charles Dismukes*

ACCESS | 📊 Metrics & More | 📖 Article Recommendations | 🗓 Supporting Information

ABSTRACT: Development of efficient electrocatalysts for the CO$_2$ reduction reaction (CO$_2$RR) to multicarbon products has been constrained by high overpotentials and poor selectivity. Here, we introduce iron phosphide (Fe$_2$P) as an earth-abundant catalyst for the CO$_2$RR to mainly C$_2$−C$_4$ products with a total CO$_2$RR Faradaic efficiency of 53% at 0 V vs RHE. Carbon product selectivity is tuned in favor of ethylene glycol formation with increasing negative bias at the expense of C$_3$−C$_4$ products. Both Grand Canonical-DFT (GC-DFT) calculations and experiments reveal that *formate, not *CO, is the initial intermediate formed from surface phosphino-hydrides and that the latter form ionic hydrides at both surface phosphorus atoms (H@P$_s$) and P-reconstructed Fe$_3$ hollow sites (H@P*). Binding of these surface hydrides weakens with negative bias (reactivity increases), which accounts for both the shift to C$_2$ products over higher C−C coupling products and the increase in the H$_2$ evolution reaction (HER) rate. GC-DFT predicts that phosphino-hydrides convert *formate to *formaldehyde, the key intermediate for C−C coupling, whereas hydrogen atoms on Fe generate tightly bound *CO via sequential PCET reactions to H$_2$O. GC-DFT predicts the peak in CO$_2$RR current density near −0.1 V is due to a local maximum in the binding affinity of *formate and *formaldehyde at this bias, which together with the more labile C$_2$ product affinity, accounts for the shift to ethylene glycol and away from C$_3$−C$_4$ products. Consistent with these predictions, addition of exogenous CO is shown to block all carbon product formation and lower the HER rate. These results demonstrate that the formation of ionic hydrides and their binding affinity, as modulated by the applied potential, controls the carbon product distribution. This knowledge provides new insight into the influence of hydride speciation and applied bias on the chemical reaction mechanism of CO$_2$RR that is relevant to all transition metal phosphides.
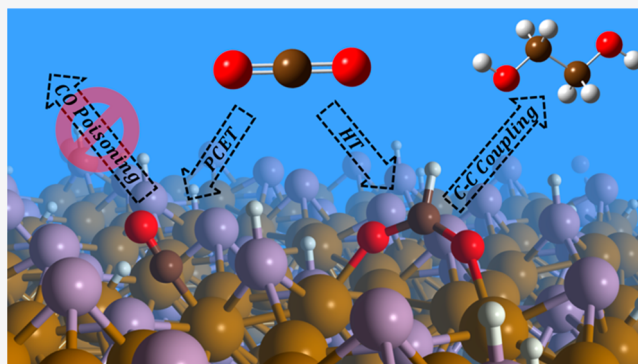
INTRODUCTION

The electrochemical reduction of waste carbon dioxide (CO$_2$RR) is a promising renewable technology for generating valuable carbon-based products, including monomers for polyethylene and polyethylene terephthalate (PET).[1,2] Commercializing this technology would aid in the replacement of petrochemicals to tackle global warming. In recent years, there have been many developments in electrocatalysis leading to high activity and selectivity for the conversion of CO$_2$ to CO,[3−11] and HCOOH.[12−20] Recent advances in catalyst doping, promotion, and supports have generated improvements in selectivity to C= products (ethylene[21−23] and ethanol[24−26]). Most state-of-the-art catalysts that facilitate C−C coupling are copper-based and produce a mixture of two or more of C$_2$H$_4$, C$_2$H$_6$, C$_2$H$_5$OH, and/or *n*-propanol.[24,27−38] However, these catalysts suffer from (1) low selectivity and lack of tunability to a single product, (2) high overpotentials, and (3) corrosion instability.

Transition metal phosphides (TMPs) are a new family of CO$_2$RR electrocatalysts that have disrupted this traditional picture and produced more complex C−C products than observed on other catalysts. Although TMPs were predicted to predominantly catalyze the H$_2$ evolution reaction (HER) at the expense of CO$_2$RR activity,[39] their high activity in C−C coupling was predicted and demonstrated specifically in the case of nickel phosphides, based on similarity to nickel-group-15 elements present in the active sites of the exergonic class of CO$_2$ reducing enzymes of acetogenic and methanogenic bacteria.[40] In particular, while Ni$_3$P is a poor CO$_2$RR catalyst and an excellent HER catalyst, both Ni$_2$P and NiP$_2$ readily
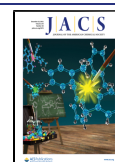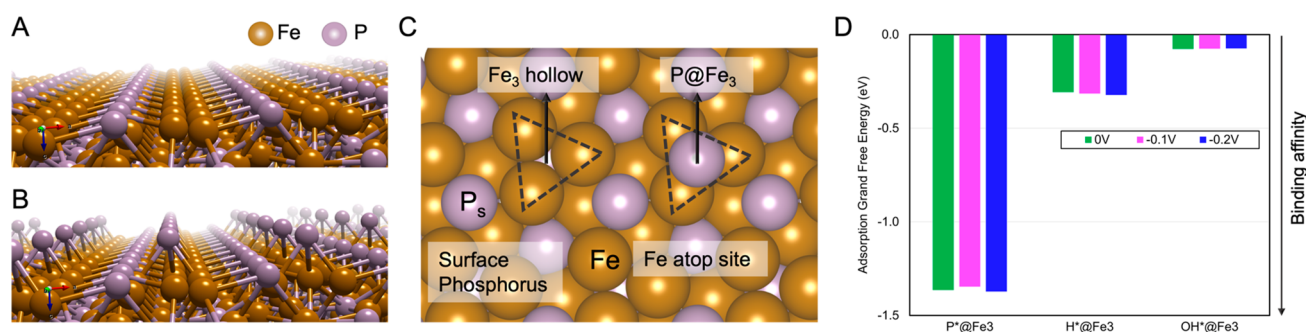
Figure 1. (A) Fe$_2$P (0001) side view showing the clean surface and (B) reconstructed surfaces. (C) Fe$_2$P (0001) top view highlighting the Fe$_3$ hollow site with and without phosphorus reconstruction. (D) Computed adsorption grand free energies (eV) vs applied electrical bias (V vs RHE, pH = 7.5) using GC-DFT. Strong adsorption of P on the Fe site shows that the surface is thermodynamically more stable when P-reconstructed (P*) than not. P* reconstruction also significantly outcompetes H and OH speciation on the Fe$_3$ site by ~1 eV. Reference states are H$_{2(aq)}$ for H*, H$_2$O$_{(aq)}$ for *OH, and bulk white phosphorus for P.

discriminate against H$_2$ formation. On Ni$_2$P, CO$_2$ is reduced to C$_4$ (2,3-furandiol) with a Faradaic efficiency of 71% at 0 V vs RHE, while, on NiP$_2$, CO$_2$ is reduced to C$_3$ (methylglyoxal) with a Faradaic efficiency of 84% at −0.10 V vs RHE. The discrimination between HER and CO$_2$RR has been attributed to different chemical mechanisms, with nickel phosphides catalyzing hydride (*H$^-$) transfer (HT) to C to produce adsorbed formate bound through its oxygen atom(s) (HCOO^{-*}), in contrast to Cu-based catalysts that have been proposed to operate via proton-coupled electron transfer (PCET) to generate carbon monoxide (*CO) as their first intermediate.[40] Density functional theory (DFT) studies produced key evidence showing that HER on nickel phosphides (e.g., on Ni$_2$P and Ni$_3$P)[41−43] proceeds through reconstructed *P adatoms that bind to native surface Ni$_3$ "hollows". These studies further predicted that at increasing negative bias below U < −0.37 V, phosphine (PH$_3$) is released from the Ni$_3$*P hollow, whereupon two additional H atoms bind to the vacant Ni$_3$ hollow, generating a Ni−H$_2$ complex prior to H$_2$ evolution.

The corresponding di-iron phosphide phase, Fe$_2$P, is iso-structural with Ni$_2$P.[44] Chemical bonding theories predict that iron should stabilize the formation of the P* adlayer more than nickel because elemental Fe atoms have two fewer electrons than Ni, and an ionization potential closer to P. Accordingly, we expect stronger binding of the P adlayer and weaker binding of surface hydrides (Fe$_3$P−H*) on Fe$_2$P than on Ni$_2$P,[45] with correspondingly higher hydride lability and potentially higher CO$_2$RR rates. Herein, we examine this hypothesis both experimentally and theoretically, through DFT calculations.

The FeP phase has been previously reported by Sun et al.[46] to selectively catalyze electrochemical CO$_2$RR toward methanol and ethanol (Faradaic efficiency of 80.2% for CH$_3$OH and 14.1% for C$_2$H$_5$OH) at −0.2 V vs RHE and low current density. They predicted that CO$_2$RR proceeds through a proton-mediated mechanism involving a bound *CO intermediate. This pathway is calculated to have a barrier as high as 2.3 eV, which is inconsistent with the low experimentally applied potentials.[46] In addition to nickel phosphides[40] and FeP,[46] other phosphides shown to catalyze CO$_2$RR are MoP[47] and Cu$_3$P[48] producing formic acid, BP[49] producing methanol, and CuP$_2$,[50] which generates 1-butanol.

Prior studies have observed electrochemical reduction of CO$_2$ to ethylene glycol (among other products) using Au,[51] Ru,[52] and Cu[2,53] as electrocatalysts at potentials more negative

than −0.58 V vs RHE.[51] Herein we report the first observation of CO$_2$ reduction to ethylene glycol using a transition metal phosphide as the electrocatalyst and achieving a major efficiency improvement by lowering the potential requirement to −0.1 V vs RHE.

In this study, we employ Grand Canonical Electronic Density Functional Theory (GC-DFT) calculations to explore the effects of applied potential on electrocatalytic activity. This state-of-the-art method models the free flow of electrons to and from the electrode to maintain the applied bias by self-consistently solving Schrodinger's equation for the system with a variable number of electrons that minimizes the grand free energy at a specified electrochemical potential. This enables the prediction of adsorption energies and surface electronic densities as a function of applied potential that traditional DFT approaches cannot access to reveal unanticipated trends.[54]

RESULTS AND DISCUSSION

Catalyst Purity and Active Surface. Phase-pure, polycrystalline iron phosphide (Fe$_2$P) was synthesized by solid state reaction at 800 °C for 24 h. The high temperature and long reaction time ensured attainment of thermodynamic facet equilibrium. Figure S1 of the Supporting Information (SI) shows that the powder X-ray diffraction pattern (PXRD) of the as-synthesized Fe$_2$P powder matches all observed peaks of the ICDD reference pattern to confirm that the catalyst was phase-pure within the technique's detection limit. Scanning electron microscopy (Figure S2) reveals the sample is polydisperse, with particle sizes ranging from 0.5 to 35 μm.

Multiple experimental and theoretical studies have shown that Ni$_2$P [0001][55,56] and therefore, by extension, iso-structural Fe$_2$P [0001] are the most stable exposed surfaces. Both Ni$_2$P and Fe$_2$P [0001] surfaces have repeating layers with M$_3$P and M$_3$P$_2$ stoichiometries, thus averaging to a total stoichiometry of M$_2$P (See Figure S3). GC-DFT with the CANDLE solvent model predicts that the Fe$_3$P$_2$-termination of the Fe$_2$P [0001] facet is more stable than the Fe$_3$P termination by approximately 0.34 J/m^2.

We investigated the surface reconstruction where phosphorus atoms adsorb at Fe$_3$ hollow sites to form the P ad-layer depicted in Figure 1A−C because there is evidence this minimizes the surface energy of transition metal phosphides.[57] Figure 1D shows the adsorption energies of H*, OH*, and P* adsorbed at the Fe$_3$ hollow site on the Fe$_3$P$_2$-terminated surface. P* has a considerably more favorable adsorption
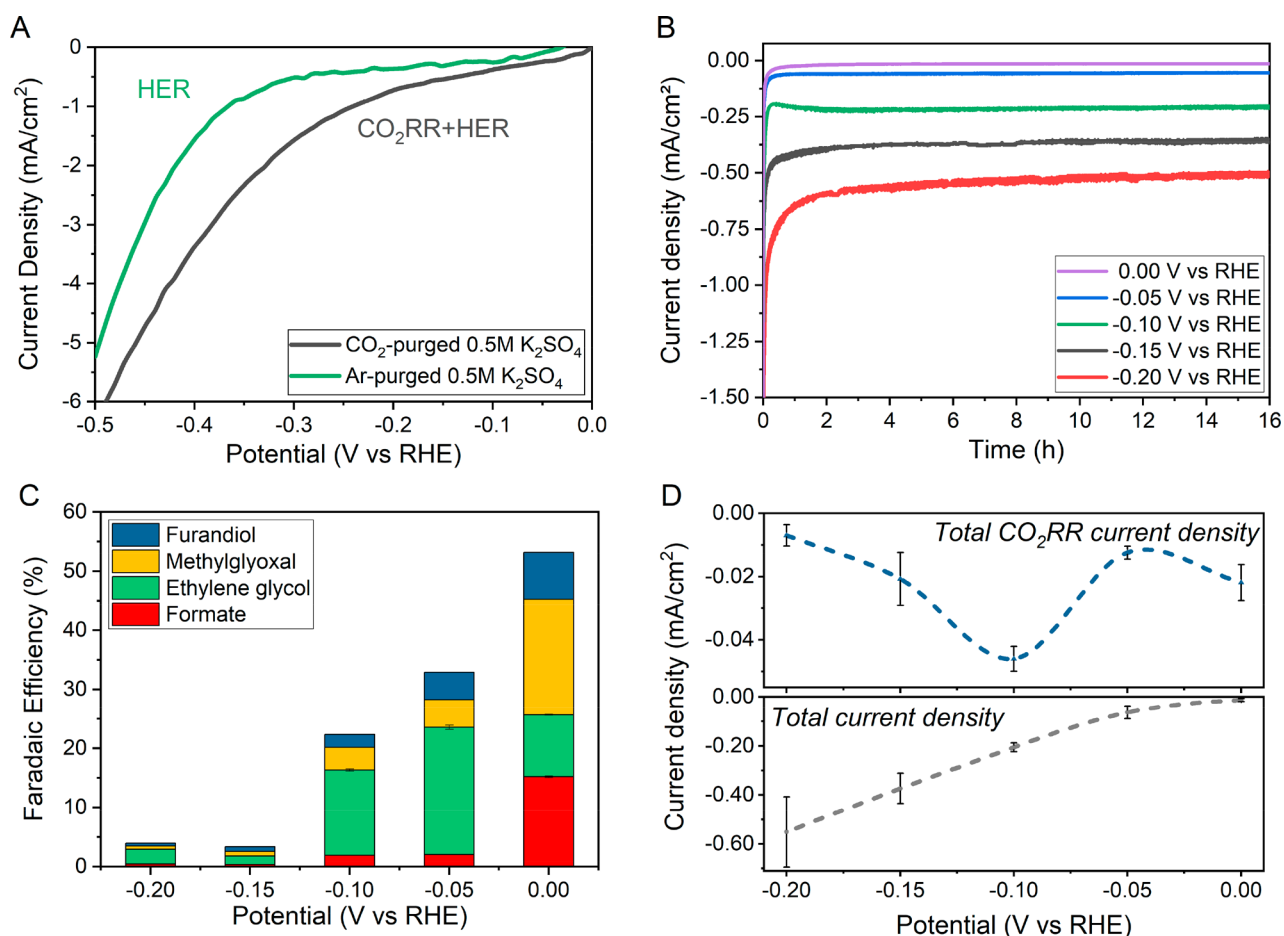
Figure 2. (A) *iR*-corrected linear sweep voltammetry of Fe_2P at 1 mV s^{-1}. Tests were conducted 0.5 M potassium sulfate under argon-purging (green), where the current density is due to HER, and under CO_2 purging (gray), where current is due to CO_2RR and HER. The current density is increased in the presence of CO_2. (B) Chronoamperometry at potentials ranging from 0 to −0.2 V on Fe_2P in CO_2-saturated 0.5 M $KHCO_3$. (C) Faradaic efficiency for CO_2RR products on an Fe_2P catalyst with a 0.5 M $KHCO_3$ electrolyte. The remaining Faradaic efficiency is hydrogen. (D) Steady-state total current density in gray and total CO_2 current density in blue (product of the CO_2RR FE and current density).

energy on the Fe_3 hollow site than H* or OH* over the investigated range of applied potentials of 0 V to −0.2 V vs RHE at pH 7.5. Thus, we conclude that the Fe_2P surface is reconstructed with a P* adlayer on Fe_3 hollow sites.

Our GC-DFT calculations indicate that P* adsorption is favored by ~1.4 eV at 100% site coverage; thus, it is likely that the entire Fe_2P [0001] facet reconstructs to form the fully P* covered surface (Figure S2). The predicted Fermi level for the fully phosphorus-reconstructed Fe_3P_2/Fe_2P [0001] surface indicates that the point of zero charge is 0.43 V vs RHE, in agreement with our measured open circuit potential of 0.45 V. Similarly, Rappe et al. found that a P* adatom is energetically favorable on analogous Ni_3 hollow sites of reconstructed Ni_2P and likely serves as the most catalytically active site for HER.[57−59] Structural reconstruction of the second and third layers was not investigated, as it is assumed that the P* reconstruction is sufficient for describing reaction energetics, as was convincingly demonstrated for the analogous Ni_2P system by Rappe et al.[57]

Surface reconstruction stabilizes Fe_2P by ~0.6 eV/site more than it stabilizes Ni_2P (Figure S4). The much stronger P* affinity on reconstructed Fe_2P is expected based on bonding considerations. Fe^0 ([Ar]3d^6 4s^2) has two fewer d-electrons than Ni^0 ([Ar] 3d^8 4s^2) and Fe_2P has a smaller energy gap between Fe and P valence orbitals than the gap between the Ni

and P valence orbitals of Ni_2P, which allows for greater hybridization. Indeed, this increase in M−P bond strength for Fe is responsible for the shorter Fe−Fe distance on Fe_2P of ~2.46 Å compared to the ~2.70 Å Ni−Ni distance on Ni_2P.

Electrochemistry. Working electrodes were prepared by mounting an Fe_2P catalyst pellet in a sandwich-type liquid electrolyte cell (as described previously[40]), where the counter and working electrodes are separated by a Nafion 115 membrane. A pressed pellet configuration was chosen to enable reproducible evaluation of the intrinsic activity of the catalyst without variability due to the electrode surface area. However, this configuration has low surface area that requires longer times for product accumulation. Higher CO_2 reduction current densities can be achieved by using gas diffusion electrodes and by nanostructuring the catalyst.

Linear sweep voltammetry was conducted in the presence and absence of CO_2 to determine the $CO_2RR+HER$ and HER activities, respectively. The results are shown in Figure 2A. At all potentials from 0 to −0.50 V, CO_2 activates a higher total current density relative to the Ar-saturated (CO_2-free) condition. Indeed, the $CO_2RR+HER$ contribution to the observed current exceeds the fraction due to HER current alone when positive of −0.40 V, while HER dominates at more negative bias. However, HER increases due to acidification by CO_2 bubbling, and so separation of HER and CO_2RR currents

by this method is not possible. The influence of exogenous carbon monoxide (CO) addition is revealing, as described later.

Representative chronoamperometry traces from 16 h experiments in 0.5 M $KHCO_3$ at a constant CO_2 flow of 5 sccm are shown in Figure 2B. The porosity of the pressed-pellet catalyst causes an initial induction period of up to 2 h during which the oxidized Fe_2P catalyst surface reduces and equilibrates with adsorbed intermediates concurrently with activation of CO_2RR current.[30] A steady-state current is reached thereafter and maintained for the remainder of the experiment. Repeating the chronoamperometry after electrolyte replacement and at any of the selected potentials with the same catalyst pellet reproduces the induction period and steady-state current. This indicates that the induction period is caused by a reversible phenomenon consistent with chemical equilibration of a porous surface with reaction intermediates under applied potential.

CO_2 Reduction Reaction Products. After application of a constant reduction potential for 16 h, the liquid products were analyzed by HPLC and ^1H NMR, while gaseous products were measured by HPLC-GC using TID and RI detection.[40] Fe_2P catalyzed the reduction of CO_2 and water to five products: formate (C_1), ethylene glycol (C_2), methylglyoxal (C_3), 2,3-furandiol (C_4), and hydrogen. All of these products—*except for ethylene glycol*—have been reported as CO_2RR products on nickel phosphide catalysts.[40] The Faradaic efficiency for total CO_2RR and for HER as a function of the applied potential are shown in Figure 2C and Figure S6, respectively. The total CO_2RR Faradaic efficiency (53%) peaks at 0.00 V and decreases with more negative biases: 33% at −0.05 V, 22% at −0.10 V, 3% at −0.15 V, and 4% at −0.20 V. Fe_2P catalyzes production of significantly more ethylene glycol (18% of CO_2RR) at potentials as low as 0.00 V vs RHE (Figure 2C). The ratio of ethylene glycol to other CO_2RR products increases to 65% at both −0.05 V and −0.10 V, although the partial currents shift to favor HER. However, we note that, in terms of electron yield, CO_2R to ethylene glycol requires 10 e^- vs 2 e^- to reduce H_2.

Figure 2D compares the total CO_2RR current density from all carbon products to the total current density (HER + CO_2RR) as a function of potential. As expected, the total current density obeys the Butler−Volmer equation with exponentially increasing current density vs applied potential. In contrast, the total CO_2RR current density increased between 0.00 V and −0.10 V to a maximum of 46 $\mu A/cm^2$, then decreases significantly to a local minimum at −0.15 V (12 $\mu A/cm^2$), followed by a slight increase at −0.20 V at the end of the range. As shown below, this response agrees with our theoretical predictions of the adsorption energies of intermediates as a function of potential. The general trend favoring CO_2RR over HER at low overpotentials suggests thermodynamic control. At increased negative bias, HER outcompetes CO_2RR due to weaker H* binding, fewer steps to the product, and phase separation of gaseous H_2, analogous to the nickel phosphides.[40] The Cn product selectivity also changes predictably with bias, as described in a later section.

Our GC-DFT calculations show that H* adsorption is possible on three unique sites on the reconstructed Fe_2P surface, which have different electronic properties (Figure 3). We find that at −0.1 V vs RHE, H* adsorption on the P* site is most endergonic (+0.33 eV), followed by the Fe site (+0.07 eV) and least endergonic on the surface P_s site (+0.01 eV).
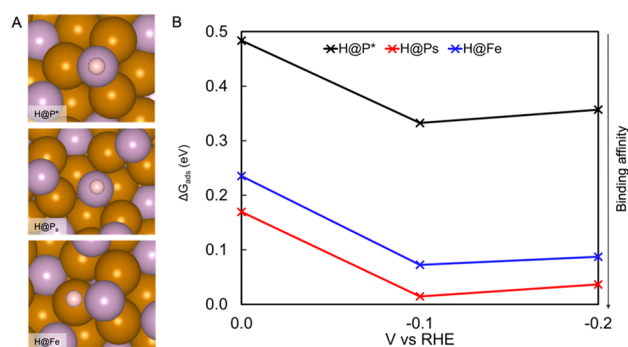

Figure 3. (A) Top-down view of H adsorption on the reconstructed P*, surface P_s, and Fe sites. (B) Adsorption grand free energies of H on the sites depicted in (A) as a function of bias. A minimum in adsorption energy (maximum in binding affinity) is observed for all three sites at −0.1 V.

Although the adsorption grand free energies are all endergonic, they are all readily thermally accessible at 300 K to facilitate CO_2RR. OH* adsorption was also investigated and found to bind less strongly to these sites compared to H*, as shown in Figure S17. The oxidation states and atomic charges obtained using Bader charge analysis are reported in Table 1. These

Table 1. Oxidation States of Adsorbed H Atoms at Three H Adsorption Sites Based on Bader Charge Analysis: Surface Phosphorus Sites (H@P_s), Reconstructed Phosphorus Sites (P*), and Surface Fe Sites (H@Fe)[a]

Oxidation States	0 V	−0.1 V	−0.2 V
H@P_s	−1.093	−1.088	−1.085
	(−0.10)	(−0.10)	(−0.11)
H@P*	−1.179	−1.177	−1.180
	(−0.27)	(−0.28)	(−0.30)
H@Fe	−0.220	−0.221	−0.225
	(−0.02)	(−0.02)	(−0.02)

[a]The sum of atomic charges of H and the atom to which it is adsorbed is indicated in parentheses.

indicate that adsorbed H on both P sites, and especially the P* adatom, are hydridic with a charge of −1 (*H^-), whereas H adsorbed on the Fe atop site has lower electron density and is nearly charge neutral. This suggests that adsorbed hydridic H* on P sites are more likely to carry out concerted two-electron hydride transfer (HT) reactions, whereas the H@Fe sites are more likely to perform one-electron hydrogen atom transfer (HAT) or PCET steps.

Figure 3B reveals that a minimum in the calculated H* adsorption free energies (maximum in the binding affinity) for all surface sites as a function of bias between 0 to −0.2 V occurs at −0.1 V vs RHE. This feature correlates well with the peak in CO_2RR current density measured at −0.1 V (Figure 2D). Taken together, this suggests that the stronger binding of hydrides at −0.1 V and their consequently longer lifetime enable the slower CO_2RR steps to compete better with the faster HER steps.

We note that the adsorption energies are referenced to H_2(aq) and so are offset relative to the solvated proton reference. As the latter energy depends on the local pH of the system at the electrode, which is unknown, we adopted the former reference. Adsorption energies referenced to dissolved

H_2 may be directly correlated to HER activity. For further discussion, see the SI.

Nonlinear electrochemical behavior, such as the changes in H* adsorption energies with applied potential shown in Figures 1D and 3B, arise from a system's intricate electronic structure and its complex dependence on bias, as shown by the projected Density of States (pDOS) plots in Figures S8–S10. As the Fermi level rises with more reducing applied potentials, population of these initially unoccupied states can result in orbital rehybridization and changes in the Helmholtz free energy, as seen in the shift and mixing of states of the pDOS near the Fermi level for the bare reconstructed surface (P*, Figure S8) but not for H adsorbed at this site (H@P*, Figure S9). Consequently, the bias changes the H* well depth and position on the grand free potential energy surface, which changes the H* binding affinity and causes the adsorbate–surface geometries to shift in response.[54] This complex interplay between surface and adsorbate states, as modified by the applied bias, is essential to understanding the features in Figures 1D and 3B and is uniquely predicted by the GC-DFT approach.

Effect of Applied Bias on CO$_2$RR and HER Selectivity. Table 2 shows the equilibrium (thermodynamic) reduction

Table 2. Standard Electrochemical Potentials at pH 7.0 of CO$_2$RR Half-Reaction Products

Product	Half-Reaction	$E^{0'}$ (V vs RHE)
Hydrogen	$2\ (e^- + H^+) \rightleftharpoons H_2$	0.00
Formic acid	$CO_2 + 2\ (e^- + H^+) \rightleftharpoons HCOOH$	−0.02
Ethylene glycol	$2\ CO_2 + 10\ (e^- + H^+) \rightleftharpoons C_2H_6O_2 + 2H_2O$	+0.20
Methylglyoxal	$3\ CO_2 + 12\ (e^- + H^+) \rightleftharpoons C_3H_4O_2 + 4\ H_2O$	+0.02
2,3-furandiol	$4\ CO_2 + 14\ (e^- + H^+) \rightleftharpoons C_4H_4O_3 + 5\ H_2O$	+0.01

potentials (E0' at pH 7.0 vs RHE) and the number of electrons required to reduce CO$_2$ to various products taken from literature data,[60,61] or calculated by Mavrovouniotis's method of individual group contributions.[62,63] This shows that ethylene glycol is predicted to be the most thermodynamically favored product by at least 0.18 V over all other products, including

H_2. Thus, we expect ethylene glycol to form unless the reactions are affected by kinetic factors such as high activation barriers or limited reactant availability. The rate of formation and dissociation of intermediates from the electrode surface and their surface mobility must be considered as entropy disfavors forming products with greater numbers of carbons.

For example, the dependence of product yields on applied potential in Figure 2C shows that at all potentials below 0 V, the C$_1$, C$_3$, and C$_4$ products are lost to formation of additional C$_2$ (ethylene glycol). Because two *C$_1$ intermediates (formic acid or formaldehyde) plus 2 equiv of *H are required to form ethylene glycol, it is apparent that the *C$_2$ precursor to produce ethylene glycol is also the precursor to the C$_3$ and C$_4$ products. The *C$_2$ aldol precursor (glycolaldehyde) simply reacts faster with *H to produce more ethylene glycol as the bias decreases than it reacts with the decreasing amount of *C$_1$ via a slower, entropically disfavored step (Figure 4). We also note that the measured free energy change for the sequential aldol coupling reactions that convert C$_1$ to C$_2$ and C$_2$ to C$_3$ aldols has a smaller driving force (~6 kJ/mol) for C$_2$ to C$_3$.[40] Thus, both entropic and possibly enthalpic terms disfavor conversion of *C$_2$ to the *C$_3$ intermediate. This simple argument explains the change in relative product yields with applied potential on Fe$_2$P, while operating via the same basic mechanism that is experimentally validated for Ni$_2$P.[40]

Figure 4 shows the proposed reaction mechanism based on our experiments and calculations, while Table S3 summarizes their equilibrium potentials from literature sources. Figure S7 details all the steps we considered and discuss next. To form ethylene glycol, methylglyoxal, and 2,3-furandiol, the reaction must undergo carbon–carbon coupling through formaldehyde, which was first proposed and experimentally verified in our previous work on Ni$_2$P[40] and confirmed by DFT calculations by Rappe et al.[64] Our GC-DFT calculations reveal that Fe$_2$P can catalyze CO$_2$RR via two possible pathways to form formaldehyde, but with very different energetics for the intermediates, as summarized in Figure 5.

Formate Pathway. The first and most likely reaction pathway based on thermodynamics proceeds by the formation of surface bound formate, shown as the pink trace in Figure 5. We identify two routes by which formate can form and bind on the surface. The first route involves a direct HT from a surface
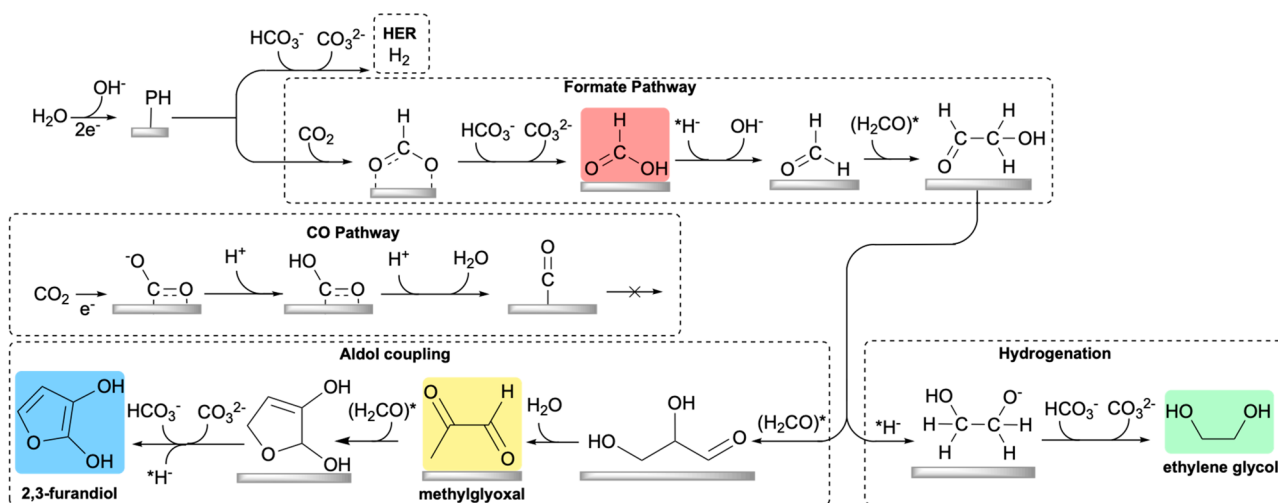

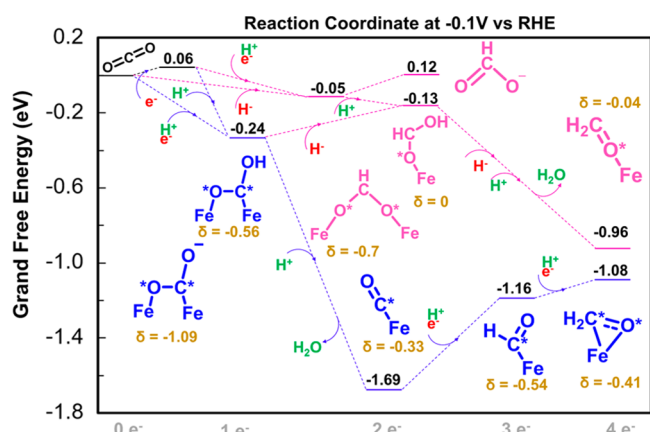**Figure 4.** Proposed mechanism for formation of CO$_2$RR products on Fe$_2$P.

Figure 5. CO₂R Reaction Coordinate Diagram via two pathways: phosphino-hydrides HT (pink) and PCET from Fe sites (blue). Grand free energies relative to aqueous CO₂ are computed using GC-DFT methods described in the SI. The sum of charge densities on all adsorbed atoms, excluding the Fe sites, are shown in gold. The HT pathway involves a surface-bound *formate intermediate, which can then desorb to yield the experimentally observed formate product or undergo further reduction to *formaldehyde. The PCET pathway goes through *COOH and *CO intermediates, followed by two more sequentially uphill PCET steps to arrive at surface-bound *formaldehyde. *CO is unusually stable and is expected to poison the surface and block or slow C product formation at operating potentials. *Formaldehyde is then assumed to undergo C−C coupling to glycolaldehyde by analogy to the experimentally verified pathway on nickel phosphides, followed by hydride transfer to ethylene glycol, as summarized in Figure 4. CO₂(aq) and H₂(aq) are used as the references for all energies computed in this figure.

hydride on the P_s or P* sites to the carbon of CO₂ to form formate aided by its coordination to a surface Fe site. Although the P_s site is more likely to be occupied by hydrides, the hydrides on the P* site are more reactive owing to their slightly higher electron density (hydricity). The Fe site, however, binds neutral H atoms (Table 1) that are less reactive in reducing aqueous CO₂ to formate. However, they can contribute to forming *formate via another route—HAT to *CO₂⁻, the surface bound anion radical. This reaction is restricted to the Fe site, in contrast to the corresponding PCET in which an electron from the surface plus a solvated proton react independently to form *formate. However, the latter PCET

pathway competes with the lower energy pathway that forms *CO and water via the outward-facing oxygen atom of *CO₂⁻, resulting in *COOH (Figure 5). GC-DFT predicts that both of these routes to formate formation are thermodynamically feasible, although transition state calculations are necessary to predict which route proceeds at faster rates.

At −0.1 V bias, formate binds to Fe via a Fe−O bond or by bridging two Fe atoms, with the bidentate geometry being energetically favored by −0.05 eV relative to CO₂ (Figure 5). Figure S18 shows that formate production becomes exergonic as the potential is swept from 0 to −0.1 V vs RHE, while the monodentate Fe binding geometry for formate production becomes exergonic at −0.2 V vs RHE. The release of bidentate formate into solution has an energy cost of 0.17 eV at −0.1 V vs RHE, which is thermodynamically accessible at 300 K and explains why formate is observed as a product, albeit at low Faradaic efficiency.

Formate is more likely to undergo protonation to form surface-bound formic acid rather than desorbing. Protonation of bidentate *formate breaks one of its two Fe−O bonds and is exergonic by 0.08 eV at −0.1 V applied bias. HT to the carbon of *HCOOH, followed by protonation of the OH group. The resulting *H₂CO−OH₂ releases a water molecule forming *formaldehyde. This reaction step is highly exergonic by 0.83− 0.96 eV, depending on the geometry of *H₂CO, which can readily undergo carbon−carbon coupling with other formaldehyde molecules on nearby Fe sites to form C₂ and higher products, as illustrated in Figure 4. The carbon−carbon coupling step was previously shown to be energetically favorable on Ni₂P,[64] although the calculations were performed using the computational hydrogen electrode (CHE) model and require further validation, for example by GC-DFT.

CO Pathway. Formaldehyde may potentially form via a *CO intermediate formed by sequential or coupled transfers of electrons and protons to CO₂, as shown by the blue trace in Figure 5. For this to occur, the surface must first bind CO₂ by transferring electron density to it to produce the anion radical *CO₂⁻ with a net charge of −1.09, as calculated by Bader charge analysis. The resulting *CO₂⁻ bridges between two Fe atoms in an Fe−C−O−Fe configuration, as illustrated in Figures 4 and 5. At −0.1 V bias, this step is endergonic by +0.06 eV and is even more endergonic at 0 and −0.2 V. Figure S19 shows that while CO₂ binding is endergonic and requires
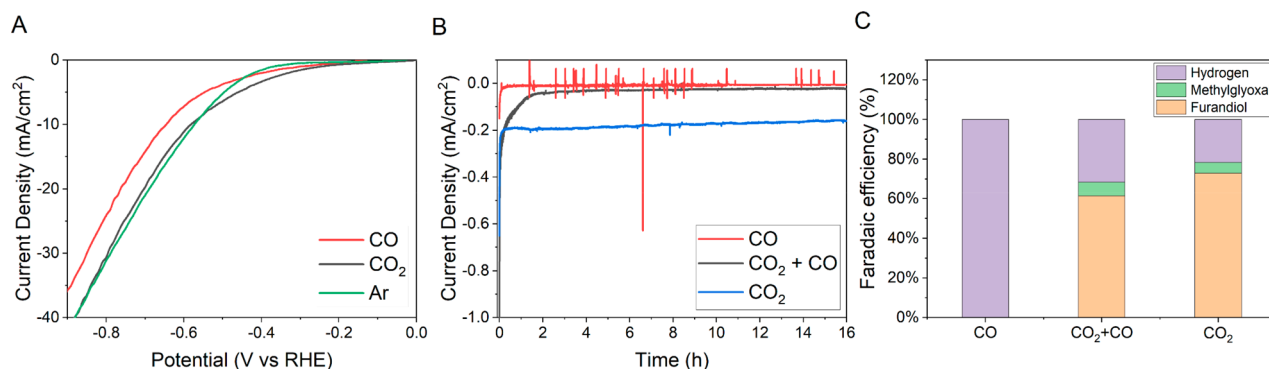

Figure 6. Carbon monoxide slow HER and CO₂RR experiments performed in 0.5 M K₂SO₄ under different purge gases. (A) Linear sweep voltammetry reveals that carbon monoxide reduces the total HER (Ar) and CO₂RR currents (CO₂). (B) Chronoamperometry at −0.1 V vs RHE for 16 h under CO, 50% CO + 50% CO₂, and CO₂, showing that current is significantly reduced in the presence of total or partial CO atmosphere. Spikes are due to noise from H₂ bubble formation. (C) Faradaic efficiency corresponding to B, showing that CO is not converted to carbon products at −0.1 V; while current is suppressed with partial CO atmosphere, there is minimal change in C product distribution.

bending of the highly stable linear CO_2 molecule, it remains kinetically accessible as our upper limit approximation of the transition state energy is computed to be ~0.5 eV. $*CO_2^-$ is then protonated to form *COOH with no significant change in the geometry as the Fe−C−O−Fe configuration remains intact. The formation of the *COOH intermediate is exergonic with a grand free energy of −0.24 eV relative to aqueous CO_2.

Because surface hydrides are readily available on nearby P_s and P* sites, *COOH could undergo an HT to form surface bound formic acid (*OCHOH) and cross over to the hydride mediated pathway described above, requiring a small energy penalty of 0.11 eV. Otherwise, *COOH can undergo another protonation and a dehydration reaction to form *CO adsorbed to an Fe site. This *CO binds strongly to the Fe site with a computed adsorption grand free energy of −1.69 eV relative to CO_2. Further conversion is suppressed by this deep binding well. Two sequential PCETs or HAT steps are necessary to form *formaldehyde from *CO via an intermediary Fe-bound *CHO. Both of those steps are sequentially uphill for a net free energy cost of +0.61 eV. This high energy cost should introduce a significant kinetic barrier, resulting in poisoning of the surface by *CO, where the Fe sites that catalyze CO_2R to formaldehyde via the formate pathway would be blocked by addition of exogenous CO. Next, we tested this prediction.

In agreement with the theoretical prediction, our experiments depicted in Figure 6 show that, under a CO atmosphere, there is no CO_2RR current observable, while the HER current is significantly suppressed. Under an atmosphere of CO and a constant applied potential of −0.1 V for 16 h, no carbon products were detected by NMR or HPLC, while hydrogen was the only detected product. At a constant applied potential of −0.1 V for 16 h, the current density is suppressed significantly under a gas mixture containing 50% CO_2 and 50% CO. The CO gas mixture partially inhibits the current, lowering the CO_2RR accumulated current (product) cumulatively by 35% relative to pure CO_2 purging, while slightly decreasing the CO_2RR Faradaic efficiency relative to HER. With a mixed CO and CO_2 atmosphere, CO produced a minor or no change in C product selectivity, indicating it neither contributes to C product formation nor modifies the CO_2-dependent pathway to products. These results show that CO is an inhibitor and that the pathway depicted in Figure 5 is a dead-end, consistent with the GC-DFT results showing high barriers to products.

Origin of the C_n Product Selectivity. The ~30% increase in the adsorption energy of bidentate formate at −0.10 V predicts that it has a longer lifetime on the catalyst surface, increasing the likelihood of a second HT to *formaldehyde, which is the obligate precursor to C−C coupling via the aldol mechanism and analogous to the mechanism on Ni_2P.[40] Indeed, the results shown in Figure 2 predict that the C_2 product dominates relative to all other observed carbon products (C_1, C_3, and C_4) at biases more negative than −0.05 V. This differs from the nickel phosphide catalysts where C_3 and C_4 products are favored at all potentials and C_2 products were not observed at all.[40] One explanation for this difference is provided by the branching reactions that separate the C_2 and C_3 pathways of the proposed mechanism (Figure 4). The C_2 branch point requires a third *hydride addition, while the C_3 branch point requires a third *formaldehyde addition. The results reported in Figure 3B show that surface hydrides bind weakly and are more labile as the bias increases from −0.1 V to −0.2 V. The resulting increase in hydride reactivity together

with the longer lifetime of adsorption of *formate favors the C_2 pathway relative to C_3 and C_4, consistent with our proposed mechanism.

Catalyst Corrosion Stability. To investigate catalyst stability, inductively coupled plasma emission spectroscopy (ICP) was conducted on the electrolyte after the 16 h catalyst activity test. These results, summarized in Table S8 and Figure S13, indicate that less than 0.2% of Fe and less than 1.5% of P consistently leached from the initially prepared electrode. This behavior is analogous to that of Ni_3P, Ni_2P, and Ni_5P_4 and is postulated to be due to the dissolution of a surface phosphor-oxide layer (formed by air exposure) after which the catalyst is stable.[58,65] This explanation is corroborated by the XPS data (Figure S14). Based on this, it is expected that the Fe and P dissolution do not indicate an inherent instability of the catalyst under working conditions. In contrast, in this study we observed that the dissolved Fe concentration depends on the applied potential, with stronger reducing potentials resulting in increased Fe dissolution. This result contradicts the thermodynamic behavior of Fe predicted by the Pourbaix diagram at pH 7.5.[66] However, at more reducing potentials, the gas-evolving HER increases exponentially causing bubble formation that could lead to Fe_2P particles dislodging from the pellet (bubbles in Figure 6). Such dislodged particles would be free to spontaneously oxidize after the cathodic bias is removed, giving rise to an increase in Fe and P concentration in solution at strong bias.

■ CONCLUSIONS

In this study we show that Fe_2P efficiently converts CO_2 primarily to ethylene glycol and to smaller amounts of formate, methylglyoxal, and 2,3-furandiol at potentials as low as 0 V vs RHE. This compares to the equally efficient CO_2RR on Ni_2P and NiP_2 which produces predominantly C_3 and C_4 products and no C_2 products.[40] GC-DFT provides an explanation for this shift.

GC-DFT reveals three features critical to CO_2RR catalysis on transition metal phosphides: (1) formation of more ionic hydrides as phosphino-hydrides that are distinctly more reactive, (2) lower free energies of hydride dissociation, and (3) higher C_1 surface affinities (*formate, *formaldehyde, and *CO) relative to C_2 and larger carbon intermediates. Consideration of these features enabled development of a mechanism that accounts for the H/C selectivity and the branching between C_2 and C_3/C_4 pathways at various applied biases. Such insight would not have been possible with the use of conventional DFT calculations and the CHE model, as it fails to consider orbital rehybridization under applied bias. Relative to the iso-structural Ni_2P catalyst, the GC-DFT computed adsorption energies of hydrides on Fe_2P are more weakly bound (more labile) owing to stronger Fe−P bonding. This result is consistent with the preferential formation of shorter C_1 and C_2 products on Fe_2P, in contrast with the longer chain C_3 and C_4 products on Ni_2P, due to the rapid termination of chain growth by hydrogenation of glycolaldehyde (the C_2 intermediate required to form C_3 and C_4 products in the mechanism). A greater hydride lability on Fe_2P also explains why the kinetically favored HER is substantially preferred on this catalyst at comparable potentials.

Through predictions from computational modeling and experimental confirmation, we show that, in contrast to copper-based catalysts, CO is not a reaction intermediate for

C_n products on Fe_2P, but instead poisons the catalyst surface. Strategies for reducing CO poisoning of transition metal phosphides may increase the intrinsic CO_2RR activity.

These results underscore the importance of surface reconstruction on both nickel and iron phosphides and the role of hydride transfer chemistry in CO_2RR that may be more generally applicable to designing new pnictide catalysts. This insight is fundamental to the discovery of new materials for the conversion of CO_2 into organic chemicals.

■ METHODS

Catalyst Synthesis. Iron metal powder (Fisher Scientific) was annealed under 1% hydrogen (balance Ar) flow for 4 h at 450 °C to remove surface oxides. The reduced iron powder was mixed with a 1.5% molar excess of red phosphorus (Alfa Aesar, 98.9%, 100 mesh), for a total of 10 g of sample per batch. The powder was ground with an agate mortar and pestle for 20 min, transferred to a quartz tube, and then flushed with argon and evacuated to less than 100 mTorr three times. The quartz tubes were sealed and heated at a rate of 0.5 °C min^{-1} stepwise to 250 °C, 450 °C, 550 °C, and finally to 800 °C. The temperature was maintained for 6 h at each intermediate step to avoid hotspot formation due to the exothermic reaction, and 24 h at the final temperature. The sample was left to cool naturally in the furnace to 60 °C. Powder X-ray diffraction (PXRD) was used to determine what/if additional amounts of phosphorus or iron were needed; these were added, and the synthesis repeated until the catalyst was phase-pure. After synthesis, the Fe_2P powder was washed in 3% HCl, stirring under argon for 2 h, to remove any soluble phosphates. The catalyst was then rinsed and centrifuged five times with water, and then twice with ethanol, followed by drying at room temperature under vacuum.

Electrochemistry. All potentials for experiments performed in this work are referenced to RHE at the pH of 7.5 used throughout this paper. Electrochemical measurements were performed in a custom-made glass-reinforced nylon-6,6 cell, with silicon O-rings and PEEK fittings (IDEX-HS) as previously described.[40] The working and counter electrodes were separated by a Nafion 115 membrane (Fuel Cell Store). Platinum black deposited on Pt foil (Alfa Aesar, 99.9%) was the counter electrode, and an ALS Hg/H_2SO_4 was used as the reference electrode, which was calibrated before each experiment against a pristine Ohaus SCE electrode. This SCE was periodically calibrated against a freshly flame-annealed Pt electrode in 0.5 M H_2SO_4 under 1 atm of H_2. The working electrode was prepared by mixing 1.400 g of the catalyst with 10% (w/w) neutralized Nafion suspension supported on an Al-mesh backing (20 × 20 mesh size, McMaster-Carr) and pressed at 22 ton onto an aluminum die (Ø = 2 cm). The die with the pressed catalyst pellet served as the working electrode and current collector, with only the Fe_2P surface exposed to the electrolyte (Figure S11). CO_2 (Air Gas, instrument grade, with a Supelco hydrocarbon trap) was supplied through the bottom of the cell to both the working and counter electrodes by a fritted gas dispersion tube (Ace Glass, 5−8 μm pore size) at a flow rate of 5 sccm (certified MKS P4B mass flow controllers). The electrolysis was run for 16 h at a time with the headspace of the working electrode compartment sampled every hour by gas chromatography. Liquid samples were collected at the end of the electrolysis (see further detail below). Each CO_2RR FE value reflects the average of at least 3 replicates.

Electrochemical measurements were performed with a Gamry 5000E potentiostat. Before each electrolysis experiment, the electrolyte (0.5 M $KHCO_3$, Sigma-Aldrich ACS reagent grade, Chelex-treated[41]) was presaturated with CO_2 for an hour. Then, a gas chromatogram was taken to ensure that no air was present in the headspace. A potentiostatic electrochemical impedance spectrum at 0 V vs RHE from 1 Hz to 1 MHz was run to determine the uncompensated resistance (typically between 6 and 10 ohms; see Figure S15). Chronoamperometry was then performed for 16 h with manual IR compensation. Between experiments, the electrochemical cell was rinsed with Millipore water, and the working electrode catalyst pellet was soaked in Millipore water for 10 min to prevent carryover of product between experiments, and then dried under a vacuum for 10 min to avoid oxidation of the catalyst surface. The catalyst pellet was reused for multiple experiments at varying potentials. By doing this, the longevity of the electrodes, particularly the working electrode, was ensured with no significant difference in product distribution observed as the electrode was reused. Additional experimental replicates using freshly made catalysts were run at all potentials to ensure that the product distribution was consistent across the investigated potential range. The electrochemical surface area was determined as described in the SI.

Gas Chromatography. Detection and quantification of possible headspace products (hydrogen, carbon monoxide, carbon dioxide, methane, ethane, and ethylene) was performed by an autosampling online HP 5890 Series II GC with a 500 μL sample loop. The GC was fitted with a 6′ packed HayeSep D, and a 6′ packed MoleSieve 13X column, with thermal conductivity and flame ionization detectors connected in series. Samples were taken before chronoamperometry to ensure that the cell was CO_2 saturated and had no air leaks, and then every hour once chronoamperometry was started. Calibration curves were constructed from certified gas standards (Gasco) by CO_2 dilution using mass flow controllers. The hydrogen calibration was done with in situ generated gas through electrolysis of water on platinum, under argon (supplied by an MFC), and diluted post-reaction with CO_2.

High-Performance Liquid Chromatography (UV/RID). Liquid products were identified and quantified by a PerkinElmer Flexar HPLC equipped with an autosampler, refractive index (RID, and UV−vis detector. An HPX-87H Aminex column (BioRad) was used with injection volumes of 10 μL. The run time was 60 min at a flow rate of 0.3 mL/min and at 65 °C. Calibration was conducted with concentration standards between 0.1 and 5 mM. The standards were: 2.3-furandiol, methylglyoxal, and ethylene glycol, in 0.5 M $KHCO_3$, detected using the RID. Acetic acid and formic acid standards were prepared at concentrations of 0.01−5 mM and detected by UV at 210 nm. Product assignment was confirmed by 1H NMR, as described in detail in the SI (Figure S17).

X-ray Photoelectron Spectroscopy (XPS). The surface of Fe_2P before and after reaction was analyzed by a Thermo K-Alpha XPS spectrometer. The chamber was evacuated to 5×10^{-9} Torr base pressure. The spectra were collected with a flood gun for charge compensation, and an X-ray beam of 400 μm was used.

Computational Methods. DFT and GC-DFT calculations with periodic boundary conditions were performed using the JDFTx code.[67] The generalized gradient approximation (GGA) was employed to compute the exchange-correlation energy using the Perdew−Burke−Ernzerhof (PBE)[68] functional combined with the SG15 Optimized Norm-Conserving Vanderbilt (ONCV) pseudopotentials to implicitly model the core electrons of the system.[69,70] The algorithm implemented by JDFTx variationally minimized the grand free energy at a set constant potential by varying the electron count within the unit cell, which were balanced by fluid bound charges (see SI for a more detailed description of GC-DFT).

The bare Fe_2P (0001) surface was modeled using a four-layer supercell consisting of alternating layers with Fe_3P_2 and Fe_3P stoichiometries, making a total of 48 Fe and 24 P atoms in the supercell to reduce undesired adsorbate−adsorbate interactions between periodic images in neighboring cells. The lattice parameters were optimized for the clean surface and fixed for all adsorbate and reconstruction calculations. A 2 × 2 × 1 Monkhorst−Pack grid was used for k-point sampling of the Brillouin zone. Geometries were optimized with a 20 hartree plane wave energy cutoff energy. The electronic energies were converged to within 1×10^{-8} hartree. Relaxation of the magnetic states resulted in the ferrimagnetic state, as expected for Fe_2P. The charge-asymmetry corrected, local-response, nonlocal-cavity solvation model (CANDLE) was implemented to account for solvation effects on molecules and surfaces.[71] An electrolyte consisting of 0.5 M Na^+ and 0.5 M F^- was embedded into the solvent model.

■ ASSOCIATED CONTENT

Ⓢ Supporting Information

The Supporting Information is available free of charge at https://pubs.acs.org/doi/10.1021/jacs.1c03428.

Characterization data of catalyst by PXRD and SEM, GC-DFT reference states and reconstruction, faradaic efficiency, current density, pDOS plots, catalyst stability assessment through ICP and XPS, ECSA, EIS, NMR, adsorption energies, and details of the calculations (PDF)

■ AUTHOR INFORMATION

Corresponding Authors

Charles B. Musgrave − *Department of Chemical and Biological Engineering, University of Colorado Boulder, Boulder, Colorado 80309, United States; Renewable and Sustainable Energy Institute, University of Colorado Boulder, Boulder, Colorado 80309, United States;* ⓞ orcid.org/0000-0002-5732-3180; Email: charles.musgrave@colorado.edu

G. Charles Dismukes − *Department of Chemistry and Chemical Biology, Rutgers, The State University of New Jersey, Piscataway, New Jersey 08854, United States; Waksman Institute of Microbiology, Rutgers, The State University of New Jersey, Piscataway, New Jersey 08854, United States;* ⓞ orcid.org/0000-0003-0155-0541; Email: dismukes@chem.rutgers.edu

Authors

Karin U. D. Calvinho − *Department of Chemistry and Chemical Biology, Rutgers, The State University of New Jersey, Piscataway, New Jersey 08854, United States;* ⓞ orcid.org/0000-0003-2078-9814

Abdulaziz W. Alherz − *Department of Chemical and Biological Engineering, University of Colorado Boulder, Boulder, Colorado 80309, United States;* ⓞ orcid.org/0000-0001-7529-3483

Kyra M. K. Yap − *Department of Chemistry and Chemical Biology, Rutgers, The State University of New Jersey, Piscataway, New Jersey 08854, United States*

Anders B. Laursen − *Department of Chemistry and Chemical Biology, Rutgers, The State University of New Jersey, Piscataway, New Jersey 08854, United States*

Shinjae Hwang − *Department of Chemistry and Chemical Biology, Rutgers, The State University of New Jersey, Piscataway, New Jersey 08854, United States;* ⓞ orcid.org/0000-0001-5442-8609

Zachary J. L. Bare − *Department of Chemical and Biological Engineering, University of Colorado Boulder, Boulder, Colorado 80309, United States*

Zachary Clifford − *Department of Chemistry and Chemical Biology, Rutgers, The State University of New Jersey, Piscataway, New Jersey 08854, United States*

Complete contact information is available at:
https://pubs.acs.org/10.1021/jacs.1c03428

Author Contributions

⊥K.U.D.C., A.W.A., and K.M.K.Y. contributed equally.

Notes

The authors declare no competing financial interest.

■ REFERENCES

(1) Jeon, H. S.; Kunze, S.; Scholten, F.; Roldan Cuenya, B. Prism-Shaped Cu Nanocatalysts for Electrochemical CO2 Reduction to Ethylene. *ACS Catal.* **2018**, *8* (1), 531−535.

(2) Kuhl, K. P.; Cave, E. R.; Abram, D. N.; Jaramillo, T. F. New Insights into the Electrochemical Reduction of Carbon Dioxide on Metallic Copper Surfaces. *Energy Environ. Sci.* **2012**, *5* (5), 7050.

(3) Asadi, M.; Kumar, B.; Behranginia, A.; Rosen, B. A.; Baskin, A.; Repnin, N.; Pisasale, D.; Phillips, P.; Zhu, W.; Haasch, R.; Klie, R. F.; Král, P.; Abiade, J.; Salehi-Khojin, A. Robust Carbon Dioxide Reduction on Molybdenum Disulphide Edges. *Nat. Commun.* **2014**, *5*, 4470.

(4) Hsieh, Y.; Senanayake, S. D.; Zhang, Y.; Xu, W.; Polyansky, D. E. Effect of Chloride Anions on the Synthesis and Enhanced Catalytic Activity of Silver Nanocoral Electrodes for CO 2 Electroreduction. *ACS Catal.* **2015**, *5* (9), 5349−5356.

(5) Rosen, B. a.; Salehi-Khojin, A.; Thorson, M. R.; Zhu, W.; Whipple, D. T.; Kenis, P. J. a.; Masel, R. I. Ionic Liquid-Mediated Selective Conversion of CO₂ to CO at Low Overpotentials. *Science* **2011**, *334* (6056), 643−644.

(6) Rosen, B. A.; Zhu, W.; Kaul, G.; Salehi-Khojin, A.; Masel, R. I.; Soc, J. E.; H-h, P.; Rosen, B. A.; Zhu, W.; Kaul, G.; Salehi-Khojin, A. Water Enhancement of CO₂ Conversion on Silver in 1-Ethyl-3-Methylimidazolium Tetrafluoroborate Service Water Enhancement of CO₂ Conversion on Silver in 1-Ethyl-3-Methylimidazolium Tetrafluoroborate. *J. Electrochem. Soc.* **2013**, *160* (2), H138.

(7) Zhu, W.; Zhang, Y.-J.; Zhang, H.; Lv, H.; Li, Q.; Michalsky, R.; Peterson, A. A.; Sun, S. Active and Selective Conversion of CO ₂ to CO on Ultrathin Au Nanowires. *J. Am. Chem. Soc.* **2014**, *136* (46), 16132−16135.

(8) Rosen, J.; Hutchings, G. S.; Lu, Q.; Forest, R. v.; Moore, A.; Jiao, F. Electrodeposited Zn Dendrites with Enhanced CO Selectivity for Electrocatalytic CO ₂ Reduction. *ACS Catal.* **2015**, *5* (8), 4586−4591.

(9) Ren, S.; Joulié, D.; Salvatore, D.; Torbensen, K.; Wang, M.; Robert, M.; Berlinguette, C. P. Molecular Electrocatalysts Can Mediate Fast, Selective CO2 Reduction in a Flow Cell. *Science* **2019**, *365* (6451), 367−369.

(10) Machan, C. W.; Chabolla, S. A.; Yin, J.; Gilson, M. K.; Tezcan, F. A.; Kubiak, C. P. Supramolecular Assembly Promotes the Electrocatalytic Reduction of Carbon Dioxide by Re(I) Bipyridine Catalysts at a Lower Overpotential. *J. Am. Chem. Soc.* **2014**, *136* (41), 14598−14607.

(11) Chen, Y.; Li, C. W.; Kanan, M. W. Aqueous CO ₂ Reduction at Very Low Overpotential on Oxide-Derived Au Nanoparticles. *J. Am. Chem. Soc.* **2012**, *134* (49), 19969−19972.

(12) Sen, S.; Liu, D.; Palmore, G. T. R. Electrochemical Reduction of CO₂ at Copper Nanofoams. *ACS Catal.* **2014**, *4* (9), 3091−3095.

(13) Hara, K.; Kudo, A.; Sakata, T. Electrochemical Reduction of Carbon Dioxide under High Pressure on Various Electrodes in an Aqueous Electrolyte. *J. Electroanal. Chem.* **1995**, *391* (1−2), 141−147.

(14) Klinkova, A.; de Luna, P.; Dinh, C. T.; Voznyy, O.; Larin, E. M.; Kumacheva, E.; Sargent, E. H. Rational Design of Efficient

Palladium Catalysts for Electroreduction of Carbon Dioxide to Formate. *ACS Catal.* **2016**, *6* (12), 8115−8120.

(15) Wang, J.; Wang, H.; Han, Z.; Han, J. Electrodeposited Porous Pb Electrode with Improved Electrocatalytic Performance for the Electroreduction of CO2 to Formic Acid. *Front. Chem. Sci. Eng.* **2015**, *9* (1), 57−63.

(16) Kortlever, R.; Peters, I.; Koper, S.; Koper, M. T. M. Electrochemical CO_2 Reduction to Formic Acid at Low Overpotential and with High Faradaic Efficiency on Carbon-Supported Bimetallic Pd-Pt Nanoparticles. *ACS Catal.* **2015**, *5* (7), 3916−3923.

(17) Riplinger, C.; Sampson, M. D.; Ritzmann, A. M.; Kubiak, C. P.; Carter, E. A. Mechanistic Contrasts between Manganese and Rhenium Bipyridine Electrocatalysts for the Reduction of Carbon Dioxide. *J. Am. Chem. Soc.* **2014**, *136* (46), 16285−16298.

(18) Clark, M. L.; Grice, K. A.; Moore, C. E.; Rheingold, A. L.; Kubiak, C. P. Electrocatalytic CO2 Reduction by M(Bpy-R)(CO)4 (M = Mo, W; R = H, TBu) Complexes. Electrochemical, Spectroscopic, and Computational Studies and Comparison with Group 7 Catalysts. *Chem. Sci.* **2014**, *5* (5), 1894−1900.

(19) Lilio, A. M.; Reineke, M. H.; Moore, C. E.; Rheingold, A. L.; Takase, M. K.; Kubiak, C. P. Incorporation of Pendant Bases into Rh(Diphosphine)₂ Complexes: Synthesis, Thermodynamic Studies, And Catalytic CO_2 Hydrogenation Activity of $[Rh(P_2 N_2)_2]$ + Complexes. *J. Am. Chem. Soc.* **2015**, *137* (25), 8251−8260.

(20) Zhang, S.; Kang, P.; Meyer, T. J. Nanostructured Tin Catalysts for Selective Electrochemical Reduction of Carbon Dioxide to Formate. *J. Am. Chem. Soc.* **2014**, *136* (5), 1734−1737.

(21) Li, F.; Thevenon, A.; Rosas-Hernández, A.; Wang, Z.; Li, Y.; Gabardo, C. M.; Ozden, A.; Dinh, C. T.; Li, J.; Wang, Y.; Edwards, J. P.; Xu, Y.; McCallum, C.; Tao, L.; Liang, Z. Q.; Luo, M.; Wang, X.; Li, H.; O'Brien, C. P.; Tan, C. S.; Nam, D. H.; Quintero-Bermudez, R.; Zhuang, T. T.; Li, Y. C.; Han, Z.; Britt, R. D.; Sinton, D.; Agapie, T.; Peters, J. C.; Sargent, E. H. Molecular Tuning of CO2-to-Ethylene Conversion. *Nature* **2020**, *577* (7791), 509−513.

(22) Jung, H.; Lee, S. Y.; Lee, C. W.; Cho, M. K.; Won, D. H.; Kim, C.; Oh, H. S.; Min, B. K.; Hwang, Y. J. Electrochemical Fragmentation of Cu 2 O Nanoparticles Enhancing Selective C-C Coupling from CO 2 Reduction Reaction. *J. Am. Chem. Soc.* **2019**, *141* (11), 4624−4633.

(23) Merino-Garcia, I.; Albo, J.; Solla-Gullón, J.; Montiel, V.; Irabien, A. Cu Oxide/ZnO-Based Surfaces for a Selective Ethylene Production from Gas-Phase CO2 Electroconversion. *Journal of CO2 Utilization* **2019**, *31*, 135−142.

(24) Song, Y.; Peng, R.; Hensley, D. K.; Bonnesen, P. v.; Liang, L.; Wu, Z.; Meyer, H. M.; Chi, M.; Ma, C.; Sumpter, B. G.; Rondinone, A. J. High-Selectivity Electrochemical Conversion of CO₂ to Ethanol Using a Copper Nanoparticle/N-Doped Graphene Electrode. *ChemistrySelect* **2016**, *1* (19), 6055−6061.

(25) Liu, Y.; Fan, X.; Nayak, A.; Wang, Y.; Shan, B.; Quan, X.; Meyer, T. J. Steering CO2 Electroreduction toward Ethanol Production by a Surface-Bound Ru Polypyridyl Carbene Catalyst on N-Doped Porous Carbon. *Proc. Natl. Acad. Sci. U. S. A.* **2019**, *116*, 26353.

(26) Ma, W.; Xie, S.; Liu, T.; Fan, Q.; Ye, J.; Sun, F.; Jiang, Z.; Zhang, Q.; Cheng, J.; Wang, Y. Electrocatalytic Reduction of CO2 to Ethylene and Ethanol through Hydrogen-Assisted C-C Coupling over Fluorine-Modified Copper. *Nature Catalysis* **2020**, *3* (6), 478−487.

(27) Hori, Y.; Kikuchi, K.; Murata, A.; Suzuki, S. Production of Methane and Ethylene in Electrochemical Reduction of Carbon Dioxide at Copper Electrode in Aqueous Hydrogencarbonate Solution. *Chem. Lett.* **1986**, *15* (6), 897−898.

(28) Ren, D.; Wong, N. T.; Handoko, A. D.; Huang, Y.; Yeo, B. S. Mechanistic Insights into the Enhanced Activity and Stability of Agglomerated Cu Nanocrystals for the Electrochemical Reduction of Carbon Dioxide to n-Propanol. *J. Phys. Chem. Lett.* **2016**, *7*, 20.

(29) Hori, Y.; Wakebe, H.; Tsukamoto, T.; Koga, O. Electrocatalytic Process Of CO Selectivity In Electrochemical Reduction Of CO2 at Metal Electrodes in Aqueous Media. *Electrochim. Acta* **1994**, *39* (11−12), 1833−1839.

(30) Chen, C. S.; Handoko, A. D.; Wan, J. H.; Ma, L.; Ren, D.; Yeo, B. S. From Chip-in-a-Lab to Lab-on-a-Chip: Towards a Single Handheld Electronic System for Multiple Application-Specific Lab-on-a-Chip (ASLOC). *Catal. Sci. Technol.* **2015**, *5*, 161.

(31) Li, Y.; Cui, F.; Ross, M. B.; Kim, D.; Sun, Y.; Yang, P. Structure-Sensitive CO2 Electroreduction to Hydrocarbons on Ultrathin 5-Fold Twinned Copper Nanowires. *Nano Lett.* **2017**, *17* (2), 1312−1317.

(32) Hori, Y.; Murata, A.; Takahashi, R. Formation of Hydrocarbons in the Electrochemical Reduction of Carbon Dioxide at a Copper Electrode in Aqueous Solution. *J. Chem. Soc., Faraday Trans. 1* **1989**, *85* (8), 2309−2326.

(33) Kas, R.; Kortlever, R.; Yılmaz, H.; Koper, M. T. M.; Mul, G. Manipulating the Hydrocarbon Selectivity of Copper Nanoparticles in CO 2 Electroreduction by Process Conditions. *ChemElectroChem* **2015**, *2* (3), 354−358.

(34) Kwon, Y.; Lum, Y.; Clark, E. L.; Ager, J. W.; Bell, A. T. CO 2 Electroreduction with Enhanced Ethylene and Ethanol Selectivity by Nanostructuring Polycrystalline Copper. *ChemElectroChem* **2016**, *3* (6), 1012−1019.

(35) Zhao, K.; Liu, Y.; Quan, X.; Chen, S.; Yu, H. CO 2 Electroreduction at Low Overpotential on Oxide-Derived Cu/ Carbons Fabricated from Metal Organic Framework. *ACS Appl. Mater. Interfaces* **2017**, *9* (6), 5302−5311.

(36) Dutta, A.; Rahaman, M.; Luedi, N.; Mohos, M.; Broekmann, P. Morphology Matters: Tuning the Product Distribution of CO₂ Electroreduction on Oxide-Derived (OD) Cu Foam Catalysts. *ACS Catal.* **2016**, *6*, 3804.

(37) Chen, C. S.; Wan, J. H.; Yeo, B. S. Electrochemical Reduction of Carbon Dioxide to Ethane Using Nanostructured Cu 2 O-Derived Copper Catalyst and Palladium(II) Chloride. *J. Phys. Chem. C* **2015**, *119* (48), 26875−26882.

(38) Ren, D.; Deng, Y.; Handoko, A. D.; Chen, C. S.; Malkhandi, S.; Yeo, B. S. Selective Electrochemical Reduction of Carbon Dioxide to Ethylene and Ethanol on Copper(I) Oxide Catalysts. *ACS Catal.* **2015**, *5* (5), 2814−2821.

(39) Landers, A. T.; Fields, M.; Torelli, D. A.; Xiao, J.; Hellstern, T. R.; Francis, S. A.; Tsai, C.; Kibsgaard, J.; Lewis, N. S.; Chan, K.; Hahn, C.; Jaramillo, T. F. The Predominance of Hydrogen Evolution on Transition Metal Sulfides and Phosphides under CO2 Reduction Conditions: An Experimental and Theoretical Study. *ACS Energy Letters* **2018**, *3* (6), 1450−1457.

(40) Calvinho, K. U. D.; Laursen, A. B.; Yap, K. M. K.; Goetjen, T. A.; Hwang, S.; Murali, N.; Mejia-Sosa, B.; Lubarski, A.; Teeluck, K. M.; Hall, E. S.; Garfunkel, E.; Greenblatt, M.; Dismukes, G. C. Selective CO2 Reduction to C3 and C4 Oxyhydrocarbons on Nickel Phosphides at Overpotentials as Low as 10 MV. *Energy Environ. Sci.* **2018**, *11* (9), 2550−2559.

(41) Laursen, A. B.; Wexler, R. B.; Whitaker, M. J.; Izett, E. J.; Calvinho, K. U. D.; Hwang, S.; Rucker, R.; Wang, H.; Li, J.; Garfunkel, E.; Greenblatt, M.; Rappe, A. M.; Dismukes, G. C. Climbing the Volcano of Electrocatalytic Activity While Avoiding Catalyst Corrosion: Ni₃P, a Hydrogen Evolution Electrocatalyst Stable in Both Acid and Alkali. *ACS Catal.* **2018**, *8* (5), 4408−4419.

(42) Wexler, R. B.; Martirez, J. M. P.; Rappe, A. M. Stable Phosphorus-Enriched (0001) Surfaces of Nickel Phosphides. *Chem. Mater.* **2016**, *28* (15), 5365−5372.

(43) Wexler, R. B.; Martirez, J. M. P.; Rappe, A. M. Active Role of Phosphorus in the Hydrogen Evolving Activity of Nickel Phosphide (0001) Surfaces. *ACS Catal.* **2017**, *7* (11), 7718−7725.
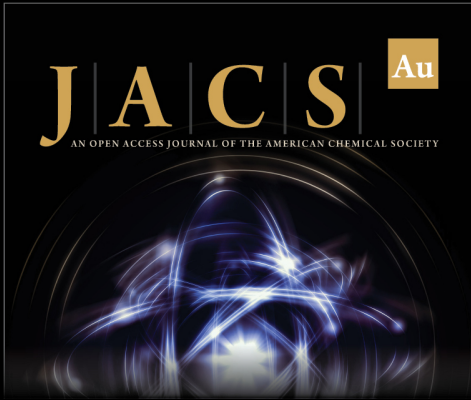
(44) International Crystal Structure Database.

(45) Wexler, R. B.; Martirez, J. M. P.; Rappe, A. M. Active Role of Phosphorus in the Hydrogen Evolving Activity of Nickel Phosphide (0001) Surfaces. *ACS Catal.* **2017**, *7*, 7718.

(46) Ji, L.; Li, L.; Ji, X.; Zhang, Y.; Mou, S.; Wu, T.; Liu, Q.; Li, B.; Zhu, X.; Luo, Y.; Shi, X.; Asiri, A. M.; Sun, X. Highly Selective Electrochemical Reduction of CO2 to Alcohols on an FeP Nanoarray. *Angew. Chem., Int. Ed.* **2020**, *59* (2), 758−762.

(47) Sun, X.; Lu, L.; Zhu, Q.; Wu, C.; Yang, D.; Chen, C.; Han, B. MoP Nanoparticles Supported on Indium-Doped Porous Carbon:

Outstanding Catalysts for Highly Efficient CO2 Electroreduction. *Angew. Chem., Int. Ed.* **2018**, *57* (9), 2427−2431.

(48) Laursen, A. B.; Calvinho, K. U. D.; Goetjen, T. A.; Yap, K. M. K.; Hwang, S.; Yang, H.; Garfunkel, E.; Dismukes, G. C. CO2 Electro-Reduction on Cu3P: Role of Cu(I) Oxidation State and Surface Facet Structure in C1-Formate Production and H2 Selectivity. *Electrochim. Acta* **2021**, *391*, 138889.

(49) Mou, S.; Wu, T.; Xie, J.; Zhang, Y.; Ji, L.; Huang, H.; Wang, T.; Luo, Y.; Xiong, X.; Tang, B.; Sun, X. Boron Phosphide Nanoparticles: A Nonmetal Catalyst for High-Selectivity Electrochemical Reduction of CO2 to CH3OH. *Adv. Mater.* **2019**, *31* (36), 1903499.

(50) Choi, M.; Bong, S.; Kim, J. W.; Lee, J. Formation of 1-Butanol from CO2 without *CO Dimerization on a Phosphorus-Rich Copper Cathode. *ACS Energy Letters* **2021**, *6* (6), 2090−2095.

(51) Tamura, J.; Ono, A.; Sugano, Y.; Huang, C.; Nishizawa, H.; Mikoshiba, S. Electrochemical Reduction of CO $_2$ to Ethylene Glycol on Imidazolium Ion-Terminated Self-Assembly Monolayer-Modified Au Electrodes in an Aqueous Solution. *Phys. Chem. Chem. Phys.* **2015**, *17* (39), 26072−26078.

(52) Tominaga, K. I.; Sasaki, Y.; Watanabe, T.; Saito, M. Ethylene Oxide-Mediated Reduction of CO2 to CO and Ethylene Glycol Catalysed by Ruthenium Complexes. *J. Chem. Soc., Chem. Commun.* **1995**, No. 15, 1489−1490.

(53) Schouten, K. J. P.; Kwon, Y.; van der Ham, C. J. M.; Qin, Z.; Koper, M. T. M. A New Mechanism for the Selectivity to C1 and C2 Species in the Electrochemical Reduction of Carbon Dioxide on Copper Electrodes. *Chemical Science* **2011**, *2* (10), 1902−1909.

(54) Alsunni, Y. A.; Alherz, A. W.; Musgrave, C. B. Electrocatalytic Reduction of CO2 to CO over Ag(110) and Cu(211) Modeled by Grand-Canonical Density Functional Theory. *J. Phys. Chem. C* **2021**, *125*, 23773.

(55) Su, L.; Cui, X.; He, T.; Zeng, L.; Tian, H.; Song, Y.; Qi, K.; Xia, B. Y. Surface Reconstruction of Cobalt Phosphide Nanosheets by Electrochemical Activation for Enhanced Hydrogen Evolution in Alkaline Solution. *Chemical Science* **2019**, *10* (7), 2019−2024.

(56) Popczun, E. J.; McKone, J. R.; Read, C. G.; Biacchi, A. J.; Wiltrout, A. M.; Lewis, N. S.; Schaak, R. E. Nanostructured Nickel Phosphide as an Electrocatalyst for the Hydrogen Evolution Reaction. *J. Am. Chem. Soc.* **2013**, *135* (25), 9267−9270.

(57) Wexler, R. B.; Martirez, J. M. P.; Rappe, A. M. Stable Phosphorus-Enriched (0001) Surfaces of Nickel Phosphides. *Chem. Mater.* **2016**, *28* (15), 5365−5372.

(58) Wexler, R. B.; Martirez, J. M. P.; Rappe, A. M. Active Role of Phosphorus in the Hydrogen Evolving Activity of Nickel Phosphide (0001) Surfaces. *ACS Catal.* **2017**, *7* (11), 7718−7725.

(59) Wexler, R. B.; Mark, J.; Martirez, P.; Rappe, A. M. Chemical Pressure-Driven Enhancement of the Hydrogen Evolving Activity of Ni $_2$ P from Nonmetal Surface Doping Interpreted via Machine Learning. *J. Am. Chem. Soc.* **2018**, *140*, 4678.

(60) Lide, D. R. *CRC Handbook of Chemistry and Physics*, 84th ed.; CRC Press: 2004.

(61) Bard, A. J.; Parsons, R.; Jordan, J. *Standard Potentials in Aqueous Solutions*; International Union of Pure and Applied Chemistry: New York, NY, 1985.

(62) Jankowski, M. D.; Henry, C. S.; Broadbelt, L. J.; Hatzimanikatis, V. Group Contribution Method for Thermodynamic Analysis of Complex Metabolic Networks. *Biophys. J.* **2008**, *95* (3), 1487−1499.

(63) Mavrovouniotis, M. L. Estimation of Standard Gibbs Energy Changes of Biotransformations. *J. Biol. Chem.* **1991**, *266* (22), 14440−14445.

(64) Banerjee, S.; Kakekhani, A.; Wexler, R. B.; Rappe, A. M. Mechanistic Insights into CO2 Electroreduction on Ni2P: Understanding Its Selectivity toward Multicarbon Products. *ACS Catal.* **2021**, *11*, 11706−11715.

(65) Laursen, A. B.; Patraju, K. R.; Whitaker, M. J.; Retuerto, M.; Sarkar, T.; Yao, N.; Ramanujachary, K. v.; Greenblatt, M.; Dismukes, G. C. Nanocrystalline Ni5P4: A Hydrogen Evolution Electrocatalyst of Exceptional Efficiency in Both Alkaline and Acidic Media. *Energy Environ. Sci.* **2015**, *8* (3), 1027−1034.

(66) Pourbaix, M. Atlas of Electrochemical Equilibria in Aqueous Solutions Version 2; 1974.

(67) Sundararaman, R.; Letchworth-Weaver, K.; Schwarz, K. A.; Gunceler, D.; Ozhabes, Y.; Arias, T. A. JDFTx: Software for Joint Density-Functional Theory. *SoftwareX* **2017**, *6*, 278−284.

(68) Perdew, J. P.; Burke, K.; Ernzerhof, M. Generalized Gradient Approximation Made Simple. *Phys. Rev. Lett.* **1996**, *77* (18), 3865.

(69) Hamann, D. R. Optimized Norm-Conserving Vanderbilt Pseudopotentials. *Phys. Rev. B: Condens. Matter Mater. Phys.* **2013**, *88* (8), 085117.

(70) Schlipf, M.; Gygi, F. Optimization Algorithm for the Generation of ONCV Pseudopotentials. *Comput. Phys. Commun.* **2015**, *196*, 36−44.

(71) Sundararaman, R.; Goddard, W. A. The Charge-Asymmetric Nonlocally Determined Local-Electric (CANDLE) Solvation Model. *J. Chem. Phys.* **2015**, *142* (6), 064107.